

Surface Gravity Fields for Asteroids and Comets

Yu Takahashi* and D. J. Scheeres†

University of Colorado at Boulder, Boulder, Colorado 80309-0429

and

Robert A. Werner‡

California Institute of Technology, Jet Propulsion Laboratory, Pasadena, California 91109

DOI: 10.2514/1.59144

The characteristics of the interior gravity field are derived, summarized, and evaluated near the surface of an asteroid for the purpose of small body proximity operations. In order to characterize the gravity field of a body, the exterior gravity field is widely in use. However, the exterior gravity field expression breaks down when computing the potential and its gradients within the Brillouin sphere, meaning that spacecraft dynamics cannot be modeled accurately in close proximity to the body's surface. On the other hand, the convergence of the potential and its gradients are guaranteed within the Brillouin sphere of the interior potential, a feature that enables the gravity field modeling near the surface of a body. After derivation, a technique for converting an exterior gravity field or a polyhedral gravity field into an interior gravity field is outlined, a method to numerically approximate the interior spherical harmonic coefficients for a body with a homogeneous density distribution is introduced, and comparisons between the spacecraft dynamics propagated in the polyhedral gravity field and the interior gravity field are made. The results show that the interior gravity field models the gravity field environment well in close proximity to the body's surface.

I. Introduction

STUDIES of small solar system bodies are listed as one of the priorities of space exploration missions. Near-Earth asteroids and comets (collectively referred to as asteroids or NEOs hereafter) are regarded as remnants that allow us to trace the evolution of the solar system. Of all the tasks performed upon a spacecraft's arrival to the asteroid, the most important is the initial characterization of the gravity field, and failure to perform this task with the desired precision in a timely manner results in a delay and shortening of the time frame dedicated for the planned scientific studies. This characterization proves particularly difficult for a highly nonspherical shape of a body represented by the majority of NEOs.

The initial estimate of the total mass of an asteroid is determined from the Doppler measurement taken during the first encounters with the asteroid. It is customary for a spacecraft to lower its orbit to better characterize the asteroid's environment, as performed by the Near Earth Asteroid Rendezvous (NEAR) Shoemaker spacecraft [1]. After this characterization phase is over, there exists a measured gravity field and a precise shape model featuring the surface morphology of the asteroid. These can be compared to each other and serve as an indicator for the homogeneity/heterogeneity in the density distribution [2]. The ultimate goal of a small-body sample return mission is the retrieval of actual specimens from the asteroid, requiring contact of a spacecraft with the asteroid's surface. Much research has been performed in support of such mission goals: the rapid characterization of the environment and orbit determination (OD) around asteroids [3,4], OD techniques and characterization of

an actual body [1,5–8], modeling of the gravity field by different approaches [9–11], efficient gravity field modeling [12–14], and proximity operations including a touch-and-go (TAG) sample return sequence [15,16].

The most commonly used expression for the gravity field is the “exterior gravity field,” or spherical harmonic gravity field, which is derived from the orthogonal spherical harmonic coefficients associated with the associated Legendre functions of degree n and order m . Equation (1) shows this exterior gravity field [17,18],

$$U(r, \phi, \lambda) = \frac{GM}{r} \left[1 + \sum_{n=1}^{\infty} \left(\frac{R^*}{r} \right)^n \sum_{m=0}^n P_{nm}(\sin \phi) \times [C_{nm} \cos(m\lambda) + S_{nm} \sin(m\lambda)] \right] \quad (1)$$

where r is the spacecraft position, ϕ is the latitude of the spacecraft, λ is the longitude of the spacecraft, G is the gravitational constant, M is the total mass of the asteroid, R^* is the reference radius, P_{nm} is the associated Legendre function of degree n and order m , and C_{nm} and S_{nm} are the spherical harmonic coefficients. Note that the spacecraft coordinates must be expressed in the body frame in Eq. (1). This exterior gravity field, as will be shown later, is valid only outside the Brillouin sphere of an asteroid (hence the name “exterior gravity field”). The Brillouin sphere can be equated with the circumscribing sphere of the asteroid within which all mass elements of the asteroid reside [19]. Thus, the exterior gravity field cannot model the dynamical environment within the Brillouin sphere, which poses a problem when, for example, performing a TAG.

There are alternatives to the exterior gravity field model, with distinct problems inherent in their expressions: the polyhedral gravity field (i.e., the shape model gravity field [9]) assumes a known density distribution, and it is necessary to prescribe either a homogeneous or a heterogeneous density distribution, the estimation of which proves difficult; the mass concentration (mascon) model is inaccurate, and estimation of each mass element renders a singularity as the number of particles is increased [20]; and the conventional expressions of the exterior gravity field and ellipsoidal gravity field fail within the Brillouin sphere/ellipsoid. To overcome these problems, the “interior gravity field” is investigated. The original work has been published by Werner [21], and the application of the theory is discussed by Takahashi and Scheeres [22]. It is the goal of this paper to combine their work with more details. To the authors' knowledge, the

Presented as Paper 12-224 at the 2012 AAS/AIAA Spaceflight Mechanics Meeting, Charleston, SC, 29 January 2012–2 February 2012; received 30 May 2012; revision received 16 August 2012; accepted for publication 16 August 2012; published online 12 February 2013. Copyright © 2012 by Yu Takahashi, D. J. Scheeres, and Robert Werner. Published by the American Institute of Aeronautics and Astronautics, Inc., with permission. Copies of this paper may be made for personal or internal use, on condition that the copier pay the \$10.00 per-copy fee to the Copyright Clearance Center, Inc., 222 Rosewood Drive, Danvers, MA 01923; include the code 1533-3884/13 and \$10.00 in correspondence with the CCC.

*Ph.D. Candidate, Aerospace Engineering Sciences, 429 UCB; yu.takahashi@colorado.edu.

†A. Richard Seebass Endowed Chair Professor, Aerospace Engineering Sciences, 429 UCB; scheeres@colorado.edu.

‡Navigation Engineer IV, Mission Design and Navigation Section, M/S 301-121, 4800 Oak Grove Drive; robert.a.werner@jpl.nasa.gov.

expression of the interior gravity field appears in the literature as early as 1948 by MacRobert [23], but MacRobert falls short of providing a fully developed description of its characteristics. The interior gravity field model is a variant of the spherical harmonic gravity field and has a comparative computational load to the conventional exterior gravity field. As will be discussed later, the convergence of the interior gravity field is guaranteed up to a particular point on the surface of the asteroid. Leveraging this property, this paper will particularly focus on a TAG mission in which a gravity expansion is only needed about one point on a body. That is, the “total mapping” of the gravity field in close proximity of the body is not studied in this paper.

The rest of the paper discusses the following materials: the derivation of the exterior and interior gravity fields; a conversion method between two gravity fields (e.g., from an exterior gravity field into an interior gravity field); a numerical approximation method to the interior spherical harmonic coefficients via shape model integration; and, finally, the comparisons between the spacecraft dynamics propagated by the interior and polyhedral gravity fields to assess their relative accuracy. A detailed derivation of the higher-order partials of the interior potential is given in the Appendix.

II. Derivation of the Exterior and Interior Gravity Fields

In this section, both the exterior and interior gravity fields are derived from the potential definition. Note that only the key steps are highlighted because Werner [21] provides a complete set.

A. Gravity Potential Definition

The potential of a field point (i.e., a spacecraft) under the influence of a body's gravity field is defined as

$$U = G \int_{\text{Volume}} \frac{\sigma(\rho)dV}{|\mathbf{r}-\boldsymbol{\rho}|} = G \int_M \frac{1}{\Delta} dm \quad (2)$$

where σ is the density as a function of the position vector of a mass element, ρ ; V is the volume; \mathbf{r} is the field point position vector; M and m are masses; and Δ is the relative position between the field point and the mass element (Fig. 1). In Fig. 1, S is the angle between \mathbf{r} and $\boldsymbol{\rho}$. By invoking the law of cosine and spherical trigonometric laws, Eq. (2) is expressed as

$$U(r, \phi, \lambda) = G \int_M \frac{1}{\Delta} dm = G \int_M \frac{1}{\sqrt{r^2 + \rho^2 - 2r\rho \cos S}} dm \quad (3)$$

The difference between the exterior and interior gravity fields arises from solving for the quantity in the square root in the integrand differently. First, the exterior gravity field is derived by factoring out r in Eq. (3),

$$U^e(r, \phi, \lambda) = G \int_M \frac{1}{r} \frac{1}{\sqrt{1 - 2\left(\frac{\rho}{r}\right) \cos S + \left(\frac{\rho}{r}\right)^2}} dm \quad (4)$$

where the superscript e denotes the exterior quantity. The reason to factor out r is related to the convergence of the Legendre polynomial, which is defined as

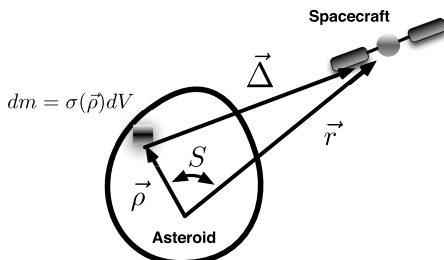


Fig. 1 Potential definition.

$$P_n(\mu) = \frac{1}{2^n n!} \frac{d^n}{d\mu^n} (\mu^2 - 1)^n \quad (5)$$

Here, $P_n(\mu)$ is the Legendre polynomial of degree n . This Legendre polynomial has the following property presented without proof:

$$\frac{1}{\sqrt{1 - 2h\mu + h^2}} = \sum_{n=0}^{\infty} h^n P_n(\mu) \quad (6)$$

which converges absolutely and uniformly when $|h| < 1$. By comparing this expression with Eq. (4), it is immediately found that $\mu = \cos S$ and $h = \rho/r$ for the exterior gravity field. Then, substitution of Eq. (6) into Eq. (4) yields

$$U^e(r, \phi, \lambda) = G \int_M \sum_{n=0}^{\infty} \frac{\rho^n}{r^{n+1}} P_n(\cos S) dm \quad (7)$$

The sphere dictated by $|h| < 1$ is called the Brillouin sphere. Thus, Eq. (7) converges when the field point is outside the Brillouin sphere: the reason U^e is called the exterior gravity field. Note that the convergence region of the exterior gravity field is dictated by the farthest mass element of the asteroid away from the coordinate center, as shown in Fig. 2.

In Fig. 2, the exterior Brillouin sphere is placed at the center of mass of the asteroid. The solid lines correspond to the region of convergence, and the dotted lines correspond to the region of mass elements that contribute to this exterior gravity field. This one-to-one correspondence seems obvious, but after the derivation of the interior gravity field, an example will be given in which it is not.

Now that the exterior gravity field is derived, a similar approach is taken to derive the interior gravity field. For the interior gravity field, Eq. (3) is revisited to factor out ρ ,

$$U^i(r, \phi, \lambda) = G \int_M \frac{1}{\rho} \frac{1}{\sqrt{1 - 2\left(\frac{r}{\rho}\right) \cos S + \left(\frac{r}{\rho}\right)^2}} dm \quad (8)$$

By observation, $\mu = \cos S$ and $h = r/\rho$ for the interior gravity field. Thus, Eq. (8) converges when the field point is closer than the mass element. That is, the interior potential converges inside a different Brillouin sphere associated with the interior expansion. By substituting Eq. (6), Eq. (8) becomes

$$U^i(r, \phi, \lambda) = G \int_M \sum_{n=0}^{\infty} \frac{r^n}{\rho^{n+1}} P_n(\cos S) dm \quad (9)$$

Note that, due to the condition of convergence dictated by $|h| < 1$, the coordinate center of the interior gravity field does not lie within the asteroid, whereas the exterior gravity field is well defined by placing the coordinate center at the center of mass of the asteroid. Figure 3 shows the convergence region of the interior gravity field.

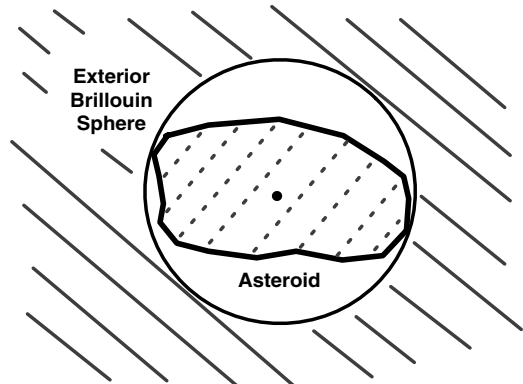


Fig. 2 Convergence region of the exterior gravity field.

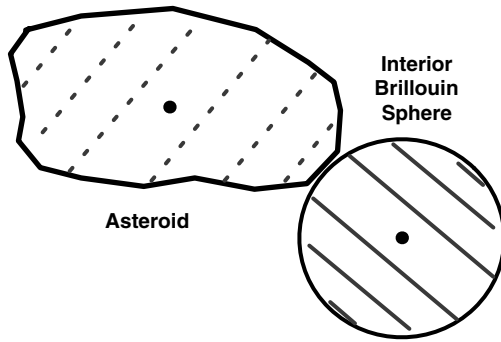


Fig. 3 Convergence region of the interior gravity field.

As with Fig. 2, the solid lines correspond to the region of convergence, and the dotted lines correspond to the region of mass elements that contribute to the interior gravity field. Again, as with the case in Fig. 2, there is one-to-one correspondence between the mass distribution and the convergence region. The only difference is that the convergence region of the interior gravity field is dictated by the closest mass element of the asteroid from the interior coordinate center. The interior coordinate center can be placed arbitrarily in space, and the performance of the interior gravity field depends on its placement. Note that the convergence of the interior gravity field is guaranteed up to a point on the surface, which, for practical purposes, is the target landing site. If a different landing site is chosen, a different interior Brillouin sphere must be constructed.

B. Convergence Region of the Exterior and Interior Gravity Fields

It has been shown that the convergence region is dictated by the farthest mass element for the exterior gravity field and by the closest one for the interior gravity field. For both gravity fields, the underlying idea is that the region of convergence should exclude any mass distribution. Now, a hypothetical situation is considered in which the two expansions are centered at the same point inside the asteroid (Fig. 4).

As the spacecraft descends, its radial distance from the center can define a spherical boundary. Some asteroid mass is entirely outside this boundary, and the rest is inside. The sphere can be taken as the Brillouin spheres for both an exterior and interior expansion centered at the same point. Mass that is inside the sphere is used in the exterior expansion, and mass that is outside is used in the interior expansion. By superimposing the two expansions, it is possible to evaluate the gravitation anywhere on the surface of the sphere. And by using a different sphere for every point on the trajectory, it is also possible to evaluate the gravitation along the entire trajectory.

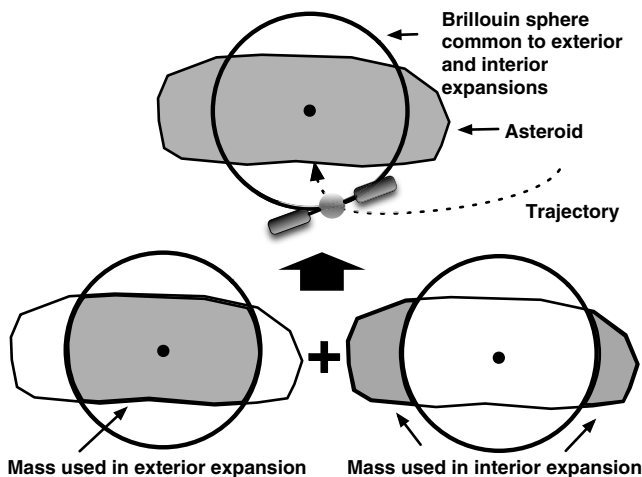


Fig. 4 Time-varying/position-dependent gravity field.

There are two obvious drawbacks. One is that the sphere size and the mass distribution outside and inside the sphere vary with spacecraft radial distance. In so many words, the spherical harmonic coefficients C_{nm} and S_{nm} of the two expansions are no longer constant and become position dependent; thus, the gravity coefficients become time-varying when motion of the spacecraft occurs. An unpublished experiment shows that the coefficients behave oddly with the radius, defying simple polynomial representations. The other drawback is that gravity will always be evaluated on the surface of the sphere, right on the boundary between the convergence/divergence regions for the two expansions. It might take high-degree expansions to evaluate gravity accurately on these boundaries.

Although interesting, this approach of coincident centers and radially varying coefficients does not seem viable. In this paper, the interior coordinate center is placed outside the body, as shown in Fig. 3 unless stated otherwise.

C. Common Convergence Region

In Fig. 5, the solid gray region (inside the interior Brillouin sphere excluding the part that lies inside the exterior Brillouin sphere) indicates the common convergence region of both the exterior and interior gravity fields. In this region, the acceleration of a field point, which is the gradient of the potential, given by the two formulas must be identical, if not the potentials themselves. Moreover, the second partial of the potential with respect to the field point position must be identical in both frames. If the second partials were not equal to each other, the two coordinate frames would have to observe different accelerations at the same location. Thus, the acceleration \mathbf{a} and the dynamics matrix $A = \partial^2 \mathbf{r} / \partial \mathbf{r}^2$ are identical in both frames. This property serves as an important tool when converting an exterior gravity field into an interior gravity field, the methodology of which will be discussed later.

D. Orientation of the Exterior and Interior Coordinates

In this section, the placement and orientation of the exterior and interior coordinate frames are discussed. In general, two vectors in different coordinate frames can be related by translation and rotation. For example, a position vector in the interior coordinate, \mathbf{r}_{int} , can be defined in terms of a position vector in the exterior coordinate, \mathbf{r}_{ext} , as

$$\mathbf{r}_{\text{sat,int}} = [IE](\mathbf{r}_{\text{sat,ext}} - \mathbf{r}_{\text{ext} \rightarrow \text{int}}) \quad (10)$$

where $\mathbf{r}_{\text{ext} \rightarrow \text{int}}$ is the vector that offsets the interior coordinate center from the exterior coordinate center, and $[IE]$ is the rotation matrix that maps the position vector in the exterior coordinate frame into that in the interior coordinate frame. One of the most convenient ways to perform the transformation is to set $[IE]$ to the identity matrix, as shown in Fig. 6.

In Fig. 6, the light gray sphere is the exterior Brillouin sphere, and the dark gray sphere is the interior Brillouin sphere just touching the asteroid's surface at the touchdown site. If so desired, one can define the interior coordinate frame relative to the touchdown site to match the gradient of the surface so that the spacecraft descends along the z axis (i.e., the local surface frame). This method requires the rotation

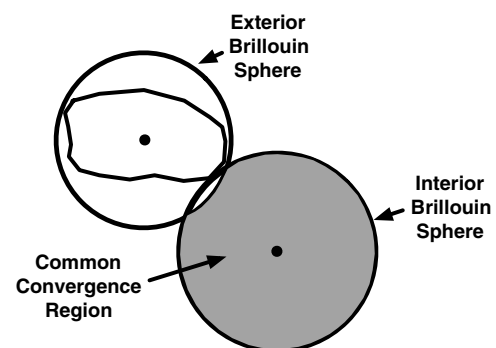


Fig. 5 Common convergence region.

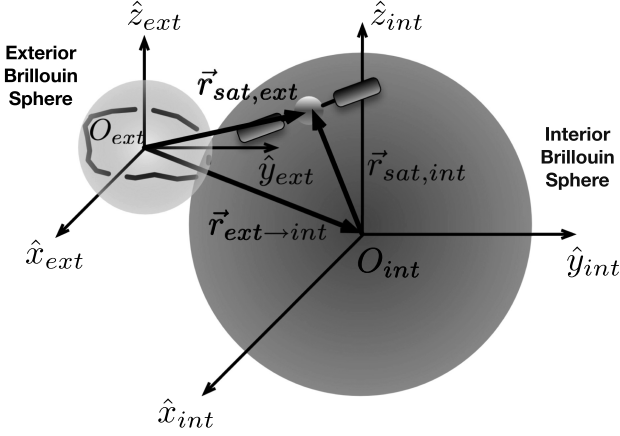


Fig. 6 Exterior and interior coordinate frames without rotation.

matrix $[IE]$ to be a nonidentity matrix but can be useful when designing a landing trajectory. In this paper, $[IE]$ is the identity matrix unless stated otherwise.

Regarding the placement of the interior coordinate center, the higher-degree and higher-order terms become important for the interior gravity field near the boundary of the Brillouin sphere; therefore, placing the interior coordinate center far from the exterior coordinate center requires accurate estimation of the higher-degree and higher-order spherical harmonic coefficients. Though not many spherical harmonic coefficients are needed to express the acceleration near the interior coordinate center, the higher-degree and higher-order coefficients become rapidly important as the spacecraft dynamics are propagated along the landing trajectory.

III. Potential as a Double Summation Expression

In this section, Eqs. (7) and (9) are rewritten in a double summation notation using the property of the Legendre polynomials. The dimensionless spherical harmonic coefficients C_{nm} and S_{nm} for the exterior and interior gravity fields are defined as

$$\begin{cases} C_{nm}^e = \frac{(2-\delta_{0,m})}{M^*} \frac{(n-m)!}{(n+m)!} \int_M \left(\frac{\rho}{R^*}\right)^n P_{nm}(\sin \phi') \cos(m\lambda') dm \\ S_{nm}^e \stackrel{m>0}{=} \frac{2}{M^*} \frac{(n-m)!}{(n+m)!} \int_M \left(\frac{\rho}{R^*}\right)^n P_{nm}(\sin \phi') \sin(m\lambda') dm \end{cases} \quad (11)$$

$$\begin{cases} C_{nm}^i = \frac{(2-\delta_{0,m})}{M^*} \frac{(n-m)!}{(n+m)!} \int_M \left(\frac{R^*}{\rho}\right)^{n+1} P_{nm}(\sin \phi') \cos(m\lambda') dm \\ S_{nm}^i \stackrel{m>0}{=} \frac{2}{M^*} \frac{(n-m)!}{(n+m)!} \int_M \left(\frac{R^*}{\rho}\right)^{n+1} P_{nm}(\sin \phi') \sin(m\lambda') dm \end{cases} \quad (12)$$

where δ is the Kronecker delta function, M^* is the reference mass, and ϕ' and λ' are the latitude and longitude of the mass element. The reference quantities (i.e., the reference mass and the reference radius) are used only to nondimensionalize the spherical harmonic coefficients, and their values do not affect the condition of convergence dictated by the ratio of r and ρ mentioned earlier. For practical purposes, it is convenient to set the reference mass as the total mass of the asteroid and the reference radius as the radius of the Brillouin sphere. However, this is not necessary, and one can arbitrarily assign the values of M^* and R^* . After expressing the Legendre polynomials in terms of the Legendre functions of degree n and order m , the double summation expressions of the two gravity fields are obtained as

$$U^e = \frac{GM^*}{R^*} \sum_{n=0}^{\infty} \sum_{m=0}^n \left(\frac{R^*}{r}\right)^{n+1} P_{nm}(\sin \phi) \begin{bmatrix} \cos(m\lambda) \\ \sin(m\lambda) \end{bmatrix} \cdot \begin{bmatrix} C_{nm}^e \\ S_{nm}^e \end{bmatrix} \quad (13)$$

$$U^i = \frac{GM^*}{R^*} \sum_{n=0}^{\infty} \sum_{m=0}^n \left(\frac{r}{R^*}\right)^n P_{nm}(\sin \phi) \begin{bmatrix} \cos(m\lambda) \\ \sin(m\lambda) \end{bmatrix} \cdot \begin{bmatrix} C_{nm}^i \\ S_{nm}^i \end{bmatrix} \quad (14)$$

In Eqs. (13) and (14), ϕ and λ are the latitude and longitude of the field point, and the dot product multiplies the cosine term with C_{nm} and the sine term with S_{nm} . The normalized spherical harmonic coefficients can also be defined, and Werner [21] presents their expressions for both exterior and interior gravity fields.

It is a well-known fact that C_{00}^e is unity when the reference mass is set to the total mass of the asteroid, the first-degree exterior spherical harmonic coefficients vanish when the coordinate center is placed at the center of mass, and the differences of the second-degree exterior spherical harmonic coefficients are linearly related to the moments of inertia of the asteroid. On the other hand, the interior spherical harmonic coefficients do not directly represent a physical character. For example, C_{00}^i is defined as

$$C_{00}^i = \frac{R^*}{M^*} \int_M \frac{1}{\rho} dm \quad (15)$$

which is a function of the location of the interior coordinate center. Interestingly enough, this C_{00}^i term does not contribute to the field point acceleration because the zeroth-degree potential is only a bias term in Eq. (14). In other words, the zeroth-degree interior gravity field does not depend on the field point position r . Unlike the exterior gravity field, the “point mass approximation” does not exist for the interior gravity field.

Even more interesting about the interior gravity field is the way that the field point acceleration interacts with the gravity field. A careful look at Eq. (13) reveals that, when the field point is placed far from the exterior coordinate center, the exterior potential is zero, and the field point acceleration can be approximated by a point mass. As the field point approaches closer to the asteroid, the field point is more susceptible to the higher-degree and higher-order terms, and the point mass assumption breaks down. On the other hand, the interior potential is identically zero when the spacecraft is placed at the interior coordinate center, and the acceleration at the interior coordinate center is constant and strictly due to the first-degree spherical harmonic coefficients. The behavior of the field point acceleration around the interior coordinate center is analogous to the field point placed far in the exterior gravity field. When the field point is placed near the boundary of the interior Brillouin sphere, the field point acceleration is more susceptible to the higher-degree and higher-order terms (analogous to the field point close to the asteroid in the exterior gravity field). Thus, errors in the interior gravity field grow as the spacecraft approaches the touchdown site.

IV. Gradient of the Interior Gravity Field

As a parameter of interest, the gradient of the interior potential is presented in this section. The gradient of the potential is the acceleration of the spacecraft, and its derivation is presented by Werner [21] in detail. Equations (16–18) provide the acceleration of a field point in the normalized interior gravity field,

$$\begin{aligned} \frac{\partial U^i}{\partial x} &= \frac{GM^*}{(R^*)^2} \sum_{n=1}^{\infty} \sum_{m=0}^n \left[\bar{C}_{nm}^i \right] \\ &\times \left[\left(-\frac{1}{2} (1 + \delta_{0,m}) \sqrt{\frac{(2-\delta_{0,m})(2n+1)}{2}} \frac{(n-m)!}{(2n-1)(n-m-2)!} \bar{b}_{n-1,m+1}^i \right. \right. \\ &\left. \left. + \frac{1}{2} \sqrt{\frac{(2-\delta_{0,m})(2n+1)}{(2-\delta_{1,m})}} \frac{(n+m)!}{(2n-1)(n+m-2)!} \bar{b}_{n-1,m-1}^i \right) \right] \end{aligned} \quad (16)$$

$$\begin{aligned} \frac{\partial U^i}{\partial y} &= \frac{GM^*}{(R^*)^2} \sum_{n=1}^{\infty} \sum_{m=0}^n \left[\begin{array}{c} \bar{S}_{nm}^i \\ -\bar{C}_{nm}^i \end{array} \right] \\ &\times \left[\left(\frac{1}{2} (1 + \delta_{0,m}) \sqrt{\frac{(2 - \delta_{0,m})(2n+1)}{2} \frac{(n-m)!}{(2n-1)(n-m-2)!}} \bar{b}_{n-1,m+1}^i \right. \right. \\ &\left. \left. + \frac{1}{2} \sqrt{\frac{(2 - \delta_{0,m})(2n+1)}{(2 - \delta_{1,m})(2n-1)} \frac{(n+m)!}{(n+m-2)!}} \bar{b}_{n-1,m-1}^i \right) \right] \end{aligned} \quad (17)$$

$$\begin{aligned} \frac{\partial U^i}{\partial z} &= \frac{GM^*}{(R^*)^2} \sum_{n=1}^{\infty} \sum_{m=0}^n \left[\begin{array}{c} \bar{C}_{nm}^i \\ \bar{S}_{nm}^i \end{array} \right] \\ &\cdot \left[\sqrt{\frac{(2n+1)}{(2n-1)} (n+m)(n-m)} \bar{b}_{n-1,m}^i \right] \end{aligned} \quad (18)$$

where the unnormalized base b_{nm}^i is defined in Eq. (A4) in the Appendix together with the derivation of the higher-order partials of the interior potential.

V. Computation of the Interior Gravity Field

In this section, the computation of the interior gravity field from a shape model and an exterior gravity field is discussed.

A. Interior Spherical Harmonic Coefficients from an Existing Shape Model

A method to approximate the interior spherical harmonic coefficients through integration over a shape model is derived. It is assumed that the shape model is precise and has high resolution and that the density is uniform. The second assumption allows for the density to be pulled out of the integrand in Eq. (12) to yield

$$\left[\begin{array}{c} C_{nm}^i \\ S_{nm}^i \end{array} \right] = \frac{1}{M^*} \int_M c_{nm}^i dm = \frac{\sigma_0}{M^*} \iiint_V c_{nm}^i dV \quad (19)$$

where σ_0 is the constant density of the body. In Eq. (19), V is the total volume of the body and shall not be confused with the volume of the interior Brillouin sphere (i.e., each spherical harmonic coefficient is a function of the mass distribution). Now, the divergence theorem is applied to Eq. (19). The divergence theorem states that

$$\iiint_V \text{div}(\mathbf{F}) dV = \iiint_V \nabla \cdot \mathbf{F} dV = \iint_S \mathbf{F} \cdot \hat{n} dA \quad (20)$$

where \hat{n} is the surface normal. Note that the divergence of a vector is only a scalar, and its value is identical irrespective of the coordinate frame chosen. To simplify Eq. (19), it is desired to find a vector \mathbf{F} such that $c_{nm}^i = \text{div}(\mathbf{F})$ (\mathbf{F} shall not be confused with the force acting on the spacecraft). To make the computation tractable, the divergence is taken in the spherical coordinates (ρ, θ, λ) which is defined as

$$\nabla \cdot \mathbf{F} = \frac{1}{\rho^2} \frac{\partial}{\partial \rho} (\rho^2 F_\rho) + \frac{1}{\rho \sin \theta} \frac{\partial}{\partial \theta} (\sin \theta F_\theta) + \frac{1}{\rho \sin \theta} \frac{\partial F_\lambda}{\partial \lambda} \quad (21)$$

where θ is the colatitude. Then, Eq. (20) is satisfied when \mathbf{F} is chosen to be

$$\mathbf{F} = F_\rho \hat{u}_\rho = -\frac{1}{n-2} \rho c_{nm}^i \hat{u}_\rho = -\frac{1}{n-2} c_{nm}^i \rho \quad (22)$$

where \hat{u}_ρ is the unit vector in the radial direction. That is,

$$c_{nm}^i = -\frac{1}{n-2} \nabla \cdot (c_{nm}^i \rho) \quad (23)$$

When $n = 2$,

$$c_{2m}^i = \nabla \cdot (\ln \rho c_{2m}^i \rho) \quad (24)$$

Thus, the integral in Eq. (19) becomes

$$\iiint_V \nabla \cdot \mathbf{F} dV = \begin{cases} -\frac{1}{n-2} \iint_S \rho c_{nm}^i \hat{u}_\rho \cdot \hat{n} dA & \text{if } n \neq 2 \\ \iint_S \rho \ln \rho c_{nm}^i \hat{u}_\rho \cdot \hat{n} dA & \text{if } n = 2 \end{cases} \quad (25)$$

The identical expression can be obtained for the normalized spherical harmonic coefficients, and replacing c_{nm}^i with \bar{c}_{nm}^i suffices. For the sake of visualization, Fig. 7 shows two tetrahedra adjacent to each other (V_1 and V_2), which are enclosed by vertices O_e, v_1, v_2, v_3 , and v_4 . Note that $\rho \hat{u}_\rho \cdot \hat{n}$ is a constant and equal to the shortest distance from the field point to the plane of the facet.

Equation (25) is hard to reduce to a simpler form. Thus, a numerical method is sought in which the integrand is approximated by the value at the center of each facet. Note that the side facet adjacent to another tetrahedron (i.e., facet $v_1 v_3 O_e$) does not contribute to the overall spherical harmonic coefficients when the density is homogeneously distributed due to the alternating signs of \hat{n} . In case each tetrahedron has a different density value, all side facets need to be considered separately. One identity that might prove useful in reducing Eq. (25) is that the interior spherical harmonic coefficients are a homogeneous function of degree $-(n+1)$. That is,

$$\rho \cdot \frac{\partial c_{nm}^i}{\partial \rho} = x \frac{\partial c_{nm}^i}{\partial x} + y \frac{\partial c_{nm}^i}{\partial y} + z \frac{\partial c_{nm}^i}{\partial z} = -(n+1) c_{nm}^i \quad (26)$$

Werner [24] leverages the property of the exterior spherical harmonic coefficients being homogeneous functions of degree n and carries out the volume integral for a unit tetrahedron after the change of coordinates. However, this approach is not suitable for the interior spherical harmonic coefficients because the integrand tends to infinity at the coordinate center.

B. Conversion Between an Exterior Gravity Field and an Interior Gravity Field

Approximation of the interior spherical harmonic coefficients via shape model integration is valid only when the density is homogeneously distributed, and this may not be the case for NEOs. After the spacecraft rendezvouses with an asteroid, the exterior gravity field is estimated through OD. Here, a technique to convert an exterior gravity field into an interior gravity field is outlined. The idea is to estimate the interior spherical harmonic coefficients that best fit the potential, acceleration, and/or dynamics matrix computed by the exterior gravity field for a collection of data points in the common convergence region. These data points are scattered within the data sphere, which defines a spherical boundary equal to or smaller than the interior Brillouin sphere in size. The data sphere is centered at the interior coordinate center, and its size is varied depending on the source data and desired accuracy of the least-squares estimation. For example, when only lower-degree interior spherical coefficients are required, a small data sphere will give sufficient accuracy. On the other hand, a large data sphere is necessary to capture the information of the higher-degree interior spherical harmonic coefficients.

As an example, a conversion method for the acceleration fitting is presented. The state vector is the interior spherical harmonic coefficients ordered in the following manner:

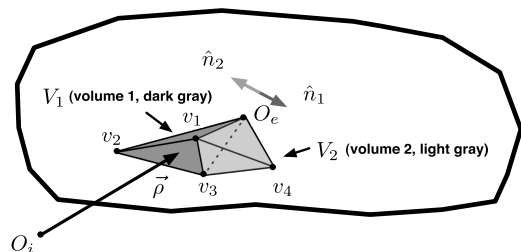


Fig. 7 Two adjacent tetrahedra.

$$[\tilde{C}_{nm}^i] = [C_{10}^i, C_{11}^i, S_{11}^i, C_{20}^i, C_{21}^i, S_{21}^i, C_{22}^i, S_{22}^i, C_{30}^i, \dots] \quad (27)$$

which consists of $n^2 + 2n$ coefficients. Note that C_{00}^i does not contribute to the field point acceleration. The objective here is to match the acceleration given by the exterior and interior gravity fields; therefore, the cost function is defined as

$$J = \frac{1}{2} \left([Q_{nm}^i][\tilde{C}_{nm}^i] - \frac{\partial U^e}{\partial \mathbf{r}_e} \right)^T W \left([Q_{nm}^i][\tilde{C}_{nm}^i] - \frac{\partial U^e}{\partial \mathbf{r}_e} \right) \quad (28)$$

where W is the weighting matrix, and $[Q_{nm}^i]$ is the partial of acceleration with respect to each interior spherical harmonic coefficient. W is chosen as the identity matrix with a scaling factor as there is no justification to weigh one component of the acceleration over the others. The dimension of $[Q_{nm}^i]$ is $[3 \times (n^2 + 2n)]$. The cost function is minimized with respect to the spherical harmonic coefficients $[\tilde{C}_{lm}^i]$ to get the normal equation

$$[\tilde{C}_{lm}^i] = ([Q_{lm}^i]^T W [Q_{lm}^i])^{-1} \left\{ [Q_{lm}^i]^T W \left(\frac{\partial U^e}{\partial \mathbf{r}_e} \right) \right\} \quad (29)$$

where the inverse term in Eq. (29) is referred to as the variance-covariance matrix. Thus, the scaling factor for W does not change the solution, but it only changes the value of the uncertainty in each estimated coefficient. Note that the acceleration at each data point gives three components. That is, the number of the data points N_{data} has to satisfy the condition $3N_{\text{data}} \geq n^2 + 2n$ in order to construct a full-rank system.

The same approach can be used to estimate both the unnormalized and normalized interior spherical harmonic coefficients by substituting the normalized components for $[\tilde{C}_{lm}^i]$ and $[Q_{lm}^i]$. Moreover, a similar least-squares fit to the potential and the dynamics matrix is also possible. For the potential fitting, the bias term plus the constant offset of the potential (treated as one parameter) needs to be estimated. For the dynamics matrix fitting, the state vector starts from the second-degree coefficients. The base gravity field model needs not be an exterior spherical harmonic gravity field; the same methodology applies to the polyhedral model, the mascon model, and any other gravity field models.

One caveat to the preceding conversion method is that there may be cases in which the common convergence region is small or even nonexistent. For instance, if a landing site is chosen to be at the neck of a binary-contact asteroid, a good portion of the region above the surface is outside the convergence region of the exterior gravity field (i.e., inside the exterior Brillouin sphere). In such cases, one may construct an initial guess of the interior spherical harmonics via shape model integration and estimate the interior spherical harmonic coefficients via OD. The study of this OD process for the interior gravity field is beyond the scope of this paper; however, it is expected that the estimation of these parameters is difficult as the spacecraft position is confined in the interior Brillouin sphere and does not get the full coverage of the dynamics.

When evaluating accuracies of the least-squares fit, it becomes quickly cumbersome to compute errors in each spherical harmonic coefficient for a large n . Thus, errors in the degree variance are defined, which are denoted as $\Delta\sigma_n^2$ as follows:

$$\Delta\sigma_n^2 = \sum_{m=0}^n (\Delta C_{nm}^2 + \Delta S_{nm}^2) \quad (30)$$

where each Δ term is computed by the estimated value minus the truth.

VI. Performance of the Interior Gravity Field

In this section, the error distribution analysis and the landing trajectory analysis are presented.

A. Error Distribution Analysis

The error distribution analysis is conducted in order to evaluate how well the interior gravity field models the acceleration and the dynamics matrix within the common convergence region of the exterior/interior gravity fields. A 15×15 exterior gravity field is numerically computed for 4769 Castalia from point masses placed at each vertex (i.e., the mascon shell model). Each mass is equal, and the sum of all masses equals the total mass of Castalia. The interior coordinate center is placed at $[0.5, 0.1, 2.5]$ km from the exterior coordinate center, which gives the interior Brillouin radius of 2.20 km. The errors are computed with 15×15 and 50×50 interior gravity fields. The benefit of working with the mascon shell model is that the spherical harmonic coefficients can be computed without error both for exterior and interior gravity fields, allowing for direct one-to-one comparisons between the two gravity fields.

The error in the acceleration is computed by the difference in magnitude, and that in the dynamics matrix is computed by the difference in determinant, which is the volume of the dyad,

$$\epsilon_{\text{acce}} = \text{abs} \left(\frac{|\mathbf{U}_{\mathbf{r}_i}^i| - |\mathbf{U}_{\mathbf{r}_e}^e|}{|\mathbf{U}_{\mathbf{r}_e}^e|} \right) \quad (31)$$

$$\epsilon_{\text{DM}} = \text{abs} \left(\frac{|\mathbf{U}_{\mathbf{r}_i \mathbf{r}_i}^i| - |\mathbf{U}_{\mathbf{r}_e \mathbf{r}_e}^e|}{|\mathbf{U}_{\mathbf{r}_e \mathbf{r}_e}^e|} \right) \quad (32)$$

Figure 8 shows the error distributions of the acceleration and the dynamics matrix for $n_{\text{int}} = 15$. In Fig. 8, the black shape at the bottom represents Castalia. The errors are computed throughout the volume of the interior Brillouin sphere with five points evenly spaced in the radial direction and 20 points evenly spaced in the longitudinal and latitudinal directions. It is shown that the errors grow radially outward as manifested in Eq. (14). Figure 9 shows the error distributions for $n_{\text{int}} = 50$. Notice the significant reduction in errors for both the acceleration and the dynamics matrix as more terms are included in the interior gravity field. However, this result reveals that the interior gravity field requires considerably more terms to accurately model the acceleration and the dynamics matrix compared with the exterior gravity field, which is one drawback of using the interior gravity field. Although the result is only shown for the mascon shell model, the same trend generally holds true for any base gravity field.

B. Landing Trajectory Analysis

The landing trajectory analysis compares the accuracy of the interior spherical harmonic coefficients estimated via a least-squares fit and those obtained via shape model integration (i.e., computed coefficients). The interior spherical harmonic coefficients are estimated up to the 40th degree using the potential, the acceleration, and the dynamics matrix data. The base gravity field model is a 15×15 exterior gravity field computed with a homogeneous density of 2.1 g/cm^3 [24], which gives the gravitational parameter of $9.4 \times 10^{-8} \text{ km}^3/\text{s}^2$. Note that this exterior gravity field is used to compute the source data (i.e., the potential, the acceleration, and the dynamics matrix) to feed into the least-squares fit as the exterior gravity field is generally the only information available about the gravity field from the OD solution in the real mission scenario. The comparison of the spacecraft trajectories is made with respect to the polyhedral gravity field as the exterior gravity field suffers from truncation errors and does not converge near the surface of the body.

The fitting algorithm is now explained. A 30×30 interior gravity field is estimated from the potential fitting, a 40×40 interior gravity field from the acceleration fitting, and another 40×40 interior gravity field from the dynamics matrix fitting. Of all the coefficients obtained from different source data types, 0 through 5th-deg coefficients are assigned from the potential estimation, 6 through 25th-deg coefficients from the acceleration estimation, and 26 through 40th-deg coefficients from the dynamics matrix estimation. The size of the data spheres is varied, all inclusive out from the interior coordinate center. The ratio of the radius of each data sphere to the interior Brillouin sphere ($R_{\text{Data}}/R_{\text{Brillouin}}$) is 0.3 for the

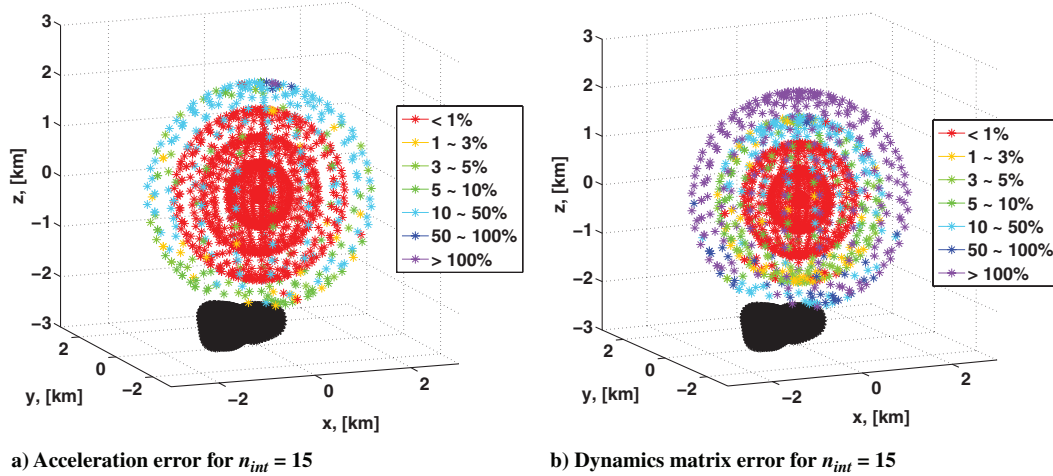


Fig. 8 a) Acceleration and b) dynamics matrix errors between the exterior and interior gravity fields with $n_{\text{ext}} = 15$ and $n_{\text{int}} = 15$.

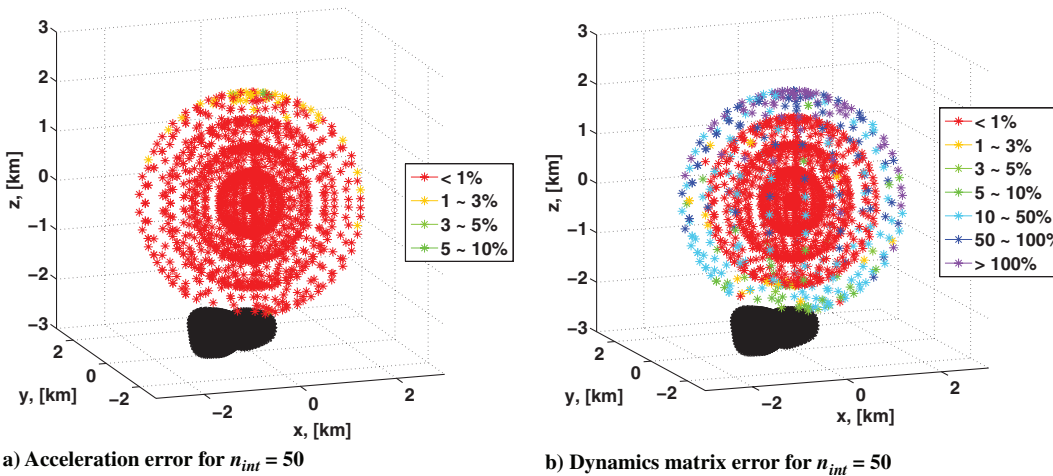


Fig. 9 a) Acceleration and b) dynamics matrix errors between the exterior and interior gravity fields with $n_{\text{ext}} = 15$ and $n_{\text{int}} = 50$.

potential, 0.8 for the acceleration, and 0.999 for the dynamics matrix. The fitting can be applied for a single source data type, but this example demonstrates that there are multiple ways of retrieving the interior gravity field. The size of the data sphere is varied since unpublished results indicate that the lower-degree coefficients are better estimated when the data sphere is smaller. When the data sphere is large, the solution of the lower-degree terms are smeared by the information from the higher-degree terms. The interior coordinate center is placed at $[-0.0615, -0.154, 2.85]$ km, which gives the interior Brillouin radius of 2.5 km, and the spacecraft is initially on the body at $[-0.344, -0.0677, 0.374]$ km in the exterior coordinates. These parameters are chosen so that the landing site is on the flat plateau of the main lobe of Castalia. The initial velocities of the spacecraft, which are identical both in the exterior and interior coordinates, are shown in Table 1.

The escape velocity at the initial spacecraft position is approximately 60 cm/s; thus, the resulting trajectories are hyperbolic. These initial conditions are propagated backward in time (i.e., negative time) for 1 h to compare how well the interior gravity field models the true polyhedral gravity field.

Figures 10a and 10b show the spacecraft trajectories sprouting from the main lobe in a hyperbolic orbit and the spacecraft distance from the interior coordinate center. In Figs. 10a and 10b, case 1 is plotted with +, case 2 with *, case 3 with o, case 4 with x, and case 5 with □. The radius of the interior Brillouin sphere is shown as a black, straight line in Fig. 10b. It is observed that the spacecraft stays within the convergence region of the interior gravity field at all times. The total travel distance range between 1.9 km (case 1) and 2.0 km (case 5).

Figure 11 shows the differences of the interior spherical harmonic coefficients estimated via a least-squares fit and those computed via shape model integration for the normalized coefficients. In Fig. 11, it is shown that the estimated spherical harmonic coefficients closely match the computed interior spherical harmonic coefficients. As will be shown shortly, both the estimated and computed spherical harmonic coefficients approximate the true polyhedral gravity field well. However, the accuracy of the estimated coefficients is heavily dependent on the accuracy of the base gravity field. In an actual small-body mission, it is a challenging task to constrain the higher-degree and higher-order spherical harmonic coefficients. The degree of the spherical harmonic coefficients that can be estimated depends on the size of the asteroid, and it is most likely that only the lower-degree coefficients can be determined.

Figure 12 shows the L_2 -norm position errors between the interior gravity fields (both estimated and computed) and the polyhedral gravity field. Again, both the computed and estimated interior gravity fields closely match the true polyhedral gravity field near the surface

Table 1 Initial velocity

Case	V_x , cm/s	V_y , cm/s	V_z , cm/s
1	0	0	-70
2	0	10	-70
3	0	-10	-70
4	10	10	-70
5	-10	-10	-70

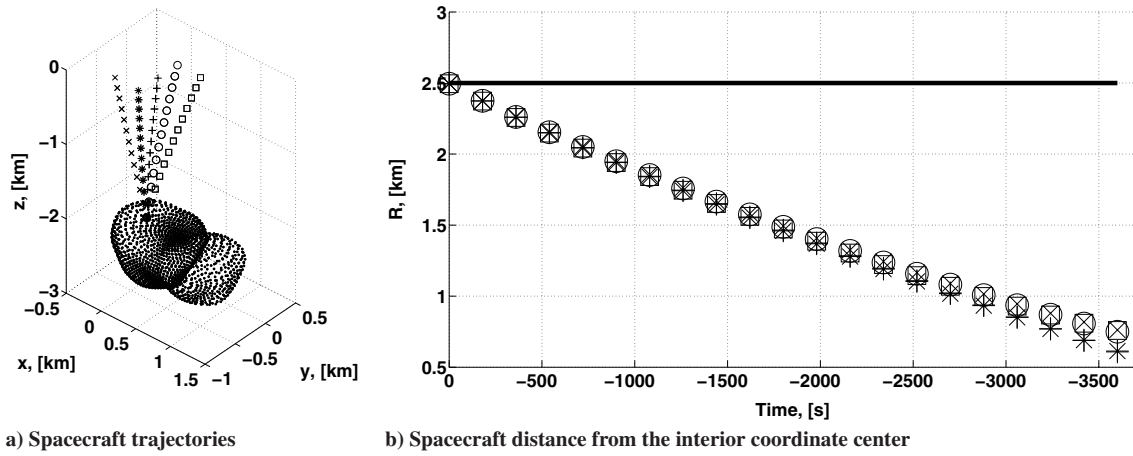


Fig. 10 Spacecraft a) trajectories in the interior coordinates and b) distance from the interior coordinate center.

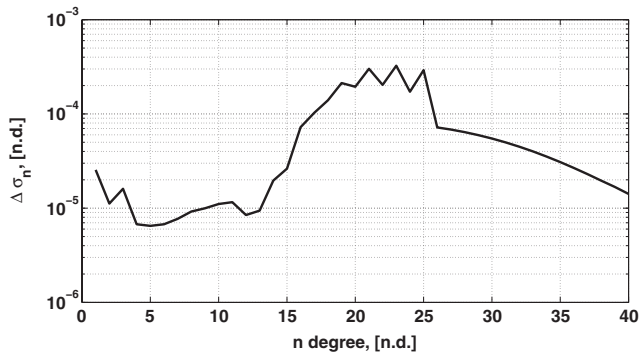
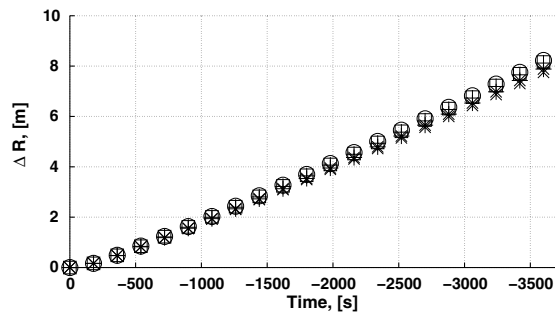
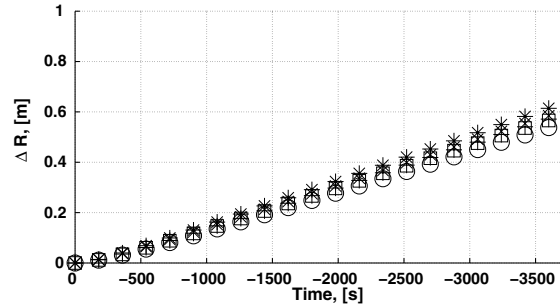


Fig. 11 Interior spherical harmonic coefficient errors with a 15×15 exterior gravity field as the source.

of the body. The position errors are less than 10 m for the estimated coefficients and several decimeters for the computed coefficients after 1 h of backward propagation. It is also worthwhile to note that the accuracy of the estimated interior spherical harmonic coefficients greatly increases when the polyhedral gravity field is used as the base gravity field (Fig. 13). In Fig. 13b, the position error has decreased to several decimeters and is comparable to Fig. 12b. The polyhedral gravity field contains no error in gravitation for a body with a homogeneous density distribution, which means that there is information of infinite-degree and order terms. In addition, convergence of the gravity field is guaranteed anywhere around the body, even on the surface, for the polyhedral gravity field. On the other hand, the exterior gravity field does not provide any information about gravitation near the surface of the body, again signifying the importance of the accuracy of the base gravity field model. All computed and estimated

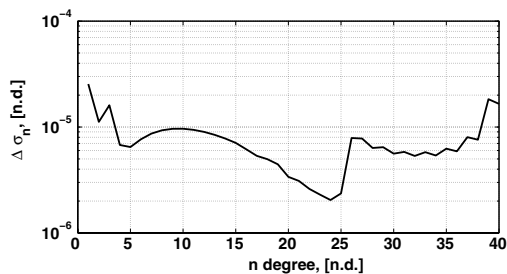


a) Position errors by the estimated interior gravity field with a 15×15 exterior gravity field as the source data

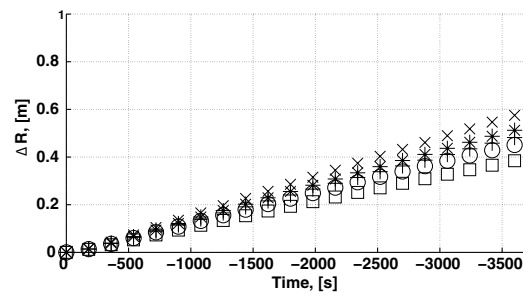


b) Position errors by the computed interior gravity field

Fig. 12 L_2 -norm position errors of the a) estimated and b) computed interior gravity fields.



a) Interior spherical harmonic coefficient errors with the polyhedral gravity field as the source



b) Position errors by the estimated interior gravity field with the polyhedral gravity field as the source data

Fig. 13 a) Interior spherical harmonic coefficient errors and b) L_2 -norm position errors with the polyhedral gravity field as the source data.

interior spherical harmonic coefficients are listed in the Appendix for reference.

VII. Conclusions

In this paper, the interior gravity field is derived, and its characteristics are discussed and applied to the proximity operation around 4769 Castalia. The interior gravity field has the convergence region within the Brillouin sphere in contrast to the exterior gravity field, for which the convergence region lies exterior to the Brillouin sphere. These two gravity fields are the mirror images of each other, and they share much commonality in their expressions.

It is shown that it is possible to convert an exterior gravity field, or any base model gravity field, into an interior gravity field through a least-squares fit. Moreover, there exists an approximation method to the interior spherical harmonic coefficients by shape model integration for a body with a homogeneous density distribution. By comparing the spacecraft trajectories computed by the polyhedral gravity field, estimated interior gravity field (least-squares fit), and computed interior gravity field (shape model integration), it is shown that both the estimated and computed interior gravity fields closely model the true polyhedral gravity field. This result indicates that the interior gravity field performs well to model the gravity field environment in close proximity to the asteroid's surface.

One possible aspect of the future work includes the total mapping of the gravity field near the surface of an asteroid, both with homogeneous and inhomogeneous density distributions, in order to apply the interior gravity field to a more generalized scenario not restricted to a touch-and-go mission. This analysis will include the optimization of the placement and sizing of the interior Brillouin sphere.

Appendix: Higher-Order Partial of the Interior Potential

In this section, the partials of the interior potential are derived, and the second-order partials of the interior potential are explicitly listed.

A. Potential as a Complex Number

It is desired to obtain the field point acceleration and the second partial of the potential for orbit determination purposes. As a matter of fact, the partial derivatives can be conveniently computed in the complex plane. As such, Eqs. (13) and (14) are rewritten in a complex number notation. First, Eq. (13) is rewritten as

$$U^e = \frac{GM^*}{R^*} \sum_{n=0}^{\infty} \sum_{m=0}^n b_{nm}^e \cdot \frac{1}{M^*} \int_M c_{nm}^e dm \quad (A1)$$

where b_{nm}^e and c_{nm}^e are defined as

$$\begin{cases} b_{nm}^e = \left(\frac{R^*}{r}\right)^{n+1} P_{nm}(\sin \phi) \begin{bmatrix} \cos(m\lambda) \\ \sin(m\lambda) \end{bmatrix} \\ c_{nm}^e = (2 - \delta_{0,m}) \frac{(n-m)!}{(n+m)!} \left(\frac{\rho}{R^*}\right)^n P_{nm}(\sin \phi') \begin{bmatrix} \cos(m\lambda') \\ \sin(m\lambda') \end{bmatrix} \end{cases} \quad (A2)$$

Similarly, Eq. (14) yields

$$U^i = \frac{GM^*}{R^*} \sum_{n=0}^{\infty} \sum_{m=0}^n b_{nm}^i \cdot \frac{1}{M^*} \int_M c_{nm}^i dm \quad (A3)$$

where b_{nm}^i and c_{nm}^i are defined as

$$\begin{cases} b_{nm}^i = \left(\frac{r}{R^*}\right)^n P_{nm}(\sin \phi) \begin{bmatrix} \cos(m\lambda) \\ \sin(m\lambda) \end{bmatrix} \\ c_{nm}^i = (2 - \delta_{0,m}) \frac{(n-m)!}{(n+m)!} \left(\frac{R^*}{\rho}\right)^{n+1} P_{nm}(\sin \phi') \begin{bmatrix} \cos(m\lambda') \\ \sin(m\lambda') \end{bmatrix} \end{cases} \quad (A4)$$

b_{nm} can be considered as a vector quantity consisting of two elements; or more conveniently, it is possible to express b_{nm}^e as a complex number,

$$\begin{aligned} b_{nm}^e &= \left(\frac{R^*}{r}\right)^{n+1} P_{nm}(\sin \phi) [\cos(m\lambda) + i \sin(m\lambda)] \\ &= \left(\frac{R^*}{r}\right)^{n+1} P_{nm}(\sin \phi) e^{im\lambda} \end{aligned} \quad (A5)$$

where i is the imaginary number that satisfies $i^2 = -1$. The same notation is used for the interior gravity field to get

$$b_{nm}^i = \left(\frac{r}{R^*}\right)^n P_{nm}(\sin \phi) e^{im\lambda} \quad (A6)$$

Then, the dot products in Eqs. (A1) and (A3) can be expressed as

$$\begin{aligned} b_{nm} \cdot \frac{1}{M^*} \int_M c_{nm} dm &= \begin{bmatrix} \Re\{b_{nm}\} \\ \Im\{b_{nm}\} \end{bmatrix} \cdot \begin{bmatrix} C_{nm} \\ S_{nm} \end{bmatrix} \\ &= C_{nm} \Re\{b_{nm}\} + S_{nm} \Im\{b_{nm}\} \end{aligned} \quad (A7)$$

This result motivates to express $1/M^* \int_M c_{nm} dm$ as a complex number by defining K_{nm} as

$$K_{nm} = C_{nm} - iS_{nm} \quad (A8)$$

such that

$$\begin{aligned} b_{nm} K_{nm} &= (C_{nm} \Re\{b_{nm}\} + S_{nm} \Im\{b_{nm}\}) \\ &+ i(-S_{nm} \Re\{b_{nm}\} + C_{nm} \Im\{b_{nm}\}) \end{aligned} \quad (A9)$$

Thus, the potential is given by the summation of the real part of the preceding expression. Note that the real part is taken at the very end of the operation, and the whole potential shall be deemed complete only when combined with the imaginary part. Using this alternative expression, Eqs. (A1) and (A3) are expressed as

$$U^e = \frac{GM^*}{R^*} \sum_{n=0}^{\infty} \sum_{m=0}^n \Re\{K_{nm}^e b_{nm}^e\} \quad (A10)$$

$$U^i = \frac{GM^*}{R^*} \sum_{n=0}^{\infty} \sum_{m=0}^n \Re\{K_{nm}^i b_{nm}^i\} \quad (A11)$$

Note that the recursive formulas derived by Werner [21] can be considered as the vector or, rather, the complex number operation. That is, b_{nm} is most easily computed by independently defining the real part of b_{nm} and the imaginary part of b_{nm} . This statement is true of c_{nm} when the spherical harmonic coefficients of a particular point mass are required. For a system of multiple point masses (i.e., the mascon model), a contribution of c_{nm} from each mass can be summed to compute the spherical harmonic coefficients of the total system,

$$C_{nm} = \frac{1}{M^*} \sum_{\kappa=1}^{\kappa_{\max}} c_{\kappa,nm} m_{\kappa} \quad (A12)$$

where κ is the index for each particle.

B. Preparation for the Partial Derivatives

In this section, the partial derivative of the potential in the Cartesian body frame, as discussed by Hotine [25], is derived. Note that only the body-frame partials are computed, and the transformation between the inertial frame and the body frame is carried out via the rotation matrix.

1. First-Order Partial

The partials of the potential are computed in the complex plane by defining two complex-conjugate variables ξ and η ,

$$\xi = x + iy \quad (A13)$$

$$\eta = x - iy \quad (\text{A14})$$

Then, $\partial/\partial x$ and $\partial/\partial y$ are given in terms of the linear combination of $\partial/\partial \xi$ and $\partial/\partial \eta$ as follows:

$$\frac{\partial}{\partial x} = \left(\frac{1}{2} \frac{\partial}{\partial x} + \frac{i}{2} \frac{\partial}{\partial y} \right) + \left(\frac{1}{2} \frac{\partial}{\partial x} - \frac{i}{2} \frac{\partial}{\partial y} \right) = \frac{\partial}{\partial \eta} + \frac{\partial}{\partial \xi} \quad (\text{A15})$$

$$\frac{\partial}{\partial y} = \mathfrak{I} \left\{ \left(\frac{1}{2} \frac{\partial}{\partial x} + \frac{i}{2} \frac{\partial}{\partial y} \right) - \left(\frac{1}{2} \frac{\partial}{\partial x} - \frac{i}{2} \frac{\partial}{\partial y} \right) \right\} = (-i) \left(\frac{\partial}{\partial \eta} - \frac{\partial}{\partial \xi} \right) \quad (\text{A16})$$

The partial with respect to z is straightforward, and no complex-number operation is necessary. Equation (A16) has significance in itself that is easy to overlook. Equation (A16) can be interpreted not only arithmetically but also geometrically. On the complex plane, the multiplication by i corresponds to a 90 deg rotation. That is, $i = (\cos \frac{\pi}{2} + i \sin \frac{\pi}{2})$, and

$$\begin{aligned} r(\cos \theta + i \sin \theta) &\xrightarrow{i} r(-\sin \theta + i \cos \theta) \\ &\xrightarrow{i} r(-\cos \theta - i \sin \theta) \xrightarrow{i} r(\sin \theta - i \cos \theta) \xrightarrow{i} \dots \end{aligned} \quad (\text{A17})$$

which is geometrically shown in Fig. A1.

By de Moivre's theorem, $-i$ corresponds to a 270 deg rotation in the complex plane: $-i = (\cos \frac{\pi}{2} + i \sin \frac{\pi}{2})^3$. Note that the y component of the vector is now in the real part of the rotated vector. Thus, multiplying through by $-i$ and taking the real part is identical to retrieving the y component of the original vector. Now, for two complex numbers A and B , AB yields

$$AB = (\Re\{A\}\Re\{B\} - \Im\{A\}\Im\{B\}) + i(\Im\{A\}\Re\{B\} + \Re\{A\}\Im\{B\}) \quad (\text{A18})$$

and multiplying through by $-i$ gives

$$\begin{aligned} (-i)AB &= (\Im\{A\}\Re\{B\} + \Re\{A\}\Im\{B\}) \\ &+ i(-\Re\{A\}\Re\{B\} + \Im\{A\}\Im\{B\}) \end{aligned} \quad (\text{A19})$$

Thus, the operation by $-i$ can be considered as not only switching from the x component to the y component but also switching the pairing of $\Re\{A\}$, $\Im\{A\}$, $\Re\{B\}$, and $\Im\{B\}$. In the potential expression, C_{nm} is tied with the real part of b_{nm} , and S_{nm} is tied with the imaginary part of b_{nm} . However, multiplication by $-i$ disbands this relationship and pairs C_{nm} with the imaginary part of b_{nm} and S_{nm} with the real part of b_{nm} .

2. Second-Order Partial

Successive applications of Eqs. (A15) and (A16) yields

$$\begin{bmatrix} \frac{\partial^2}{\partial x^2} & \frac{\partial^2}{\partial y \partial x} \\ \frac{\partial^2}{\partial x \partial y} & \frac{\partial^2}{\partial y^2} \end{bmatrix} = \begin{bmatrix} \left(\frac{\partial^2}{\partial \eta^2} + 2 \frac{\partial^2}{\partial \eta \partial \xi} + \frac{\partial^2}{\partial \xi^2} \right) & (-i) \left(\frac{\partial^2}{\partial \eta^2} - \frac{\partial^2}{\partial \xi^2} \right) \\ (-i) \left(\frac{\partial^2}{\partial \eta^2} - \frac{\partial^2}{\partial \xi^2} \right) & - \left(\frac{\partial^2}{\partial \eta^2} - 2 \frac{\partial^2}{\partial \eta \partial \xi} + \frac{\partial^2}{\partial \xi^2} \right) \end{bmatrix} \quad (\text{A20})$$

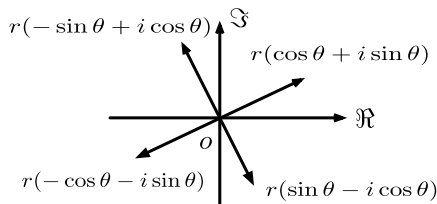


Fig. A1 90 deg rotation in the complex plane.

$$\begin{bmatrix} \frac{\partial^2}{\partial x \partial z} \\ \frac{\partial^2}{\partial y \partial z} \end{bmatrix} = \begin{bmatrix} \frac{\partial^2}{\partial \eta \partial z} + \frac{\partial^2}{\partial \xi \partial z} \\ (-i) \left(\frac{\partial^2}{\partial \eta \partial z} - \frac{\partial^2}{\partial \xi \partial z} \right) \end{bmatrix} \quad (\text{A21})$$

where assumption is made that $\frac{\partial^2}{\partial \eta \partial \xi} = \frac{\partial^2}{\partial \xi \partial \eta}$ for a smooth continuous function.

C. Complex Conjugate Partial

The expressions of the higher-order partial derivatives are derived. The theory discussed here is based on the work by Cunningham [26]. The theory of complex conjugates rectifies the oversight made earlier when taking the partials. The overlook made is that a p th-order derivative of the associated Legendre function of order m yields an $(m-p)$ th-order associated Legendre function, which is simply treated as zero when $m-p < 0$. However, the resultant $(m-p)$ th-order associated Legendre function is nonzero, as claimed by Cunningham, due to the property of the complex variables. Cunningham's method is described both for the exterior and interior gravity fields by Takahashi and Scheeres [22]; however, in this paper, only the higher-order partials for the interior gravity field are derived.

First, the operators P and M are defined as

$$P = 2 \frac{\partial}{\partial \eta} = \frac{\partial}{\partial x} + i \frac{\partial}{\partial y} \quad (\text{A22})$$

$$M = 2 \frac{\partial}{\partial \xi} = \frac{\partial}{\partial x} - i \frac{\partial}{\partial y} \quad (\text{A23})$$

The important characteristic of P and M applied to the potential expression is that, when $PM = MP$ is applied, the expression reduces to the negative of the second-order partial with respect to z because of the Laplace equation,

$$(PM)U = \left(\frac{\partial^2}{\partial x^2} + \frac{\partial^2}{\partial y^2} \right) U = - \left(\frac{\partial^2}{\partial z^2} \right) U \quad (\text{A24})$$

By leveraging the results by Werner [21], it can be shown that

$$P^s b_{nm}^i = \left(\frac{\partial}{\partial x} + i \frac{\partial}{\partial y} \right)^s b_{nm}^i = (-1)^s \left(\frac{1}{R^*} \right)^s b_{n-s, m+s}^i \quad (\text{A25})$$

$$M^q b_{nm}^i = \left(\frac{\partial}{\partial x} - i \frac{\partial}{\partial y} \right)^q b_{nm}^i = \frac{(n+m)!}{(n+m-2q)!} \left(\frac{1}{R^*} \right)^q b_{n-q, m-q}^i \quad (\text{A26})$$

$$\frac{\partial^\gamma b_{nm}^i}{\partial z^\gamma} = \frac{(n+m)!}{(n+m-\gamma)!} \left(\frac{1}{R^*} \right)^\gamma b_{n-\gamma, m}^i \quad (\text{A27})$$

where Eq. (A26) is defined only when $m \geq q$. When $m < q$, Eq. (A26) is rearranged to obtain

$$\begin{aligned} M^q b_{nm}^i &= \left(\frac{\partial}{\partial x} - i \frac{\partial}{\partial y} \right)^q b_{nm}^i \\ &= \left(\frac{\partial}{\partial x} - i \frac{\partial}{\partial y} \right)^{q-m} \left(\frac{\partial}{\partial x} - i \frac{\partial}{\partial y} \right)^m b_{nm}^i \\ &= \left(\frac{\partial}{\partial x} - i \frac{\partial}{\partial y} \right)^{q-m} \frac{(n+m)!}{(n-m)!} \left(\frac{1}{R^*} \right)^m b_{n-m, 0}^i \end{aligned} \quad (\text{A28})$$

Note that the zeroth order of b^i contains only z and r^2 , and successive applications of P and M for this type of function yield a conjugate pair g and \tilde{g} ,

$$\left(\frac{\partial}{\partial x} + i \frac{\partial}{\partial y} \right)^p f(z, r^2) = P^p f(z, r^2) = 2^p (x + iy)^p \frac{\partial^p f}{\partial (r^2)^p} = g \quad (\text{A29})$$

Table A1 Computed normalized interior spherical harmonic coefficients (Sec. V.A)

Degree	Order	\bar{C}^i coefficients	\bar{S}^i coefficients
n	m	\bar{C}_{nm}^i	\bar{S}_{nm}^i
1	0	-0.4294875615	—
1	1	$8.120673749 \times 10^{-3}$	$2.303011756 \times 10^{-2}$
2	0	0.2822870503	—
2	1	$-8.505578460 \times 10^{-3}$	$-2.640537399 \times 10^{-2}$
2	2	$2.978959177 \times 10^{-3}$	$4.621403642 \times 10^{-4}$
3	0	-0.2002014182	—
3	1	$7.633131661 \times 10^{-3}$	$2.682639552 \times 10^{-2}$
3	2	$-4.791030429 \times 10^{-3}$	$-6.855587939 \times 10^{-4}$
3	3	$1.976597828 \times 10^{-4}$	$3.152131075 \times 10^{-4}$
4	0	0.1463890291	—
4	1	$-6.164070060 \times 10^{-3}$	$-2.57311274 \times 10^{-2}$
4	2	$6.166920346 \times 10^{-3}$	$7.875589106 \times 10^{-4}$
4	3	$-3.842986975 \times 10^{-4}$	$-6.205334437 \times 10^{-4}$
4	4	$1.799867656 \times 10^{-5}$	$2.482523910 \times 10^{-5}$

Table A2 Estimated normalized interior spherical harmonic coefficients with the polyhedral gravity field as the source data (Sec. V.B)

Degree	Order	\bar{C}^i coefficients	\bar{S}^i coefficients
n	m	\bar{C}_{nm}^i	\bar{S}_{nm}^i
1	0	-0.4295276518	—
1	1	$8.133916153 \times 10^{-3}$	$2.304298876 \times 10^{-2}$
2	0	0.2823032008	—
2	1	$-8.517830861 \times 10^{-3}$	$-2.641977190 \times 10^{-2}$
2	2	$2.980728434 \times 10^{-3}$	$4.644069596 \times 10^{-4}$
3	0	-0.2001687433	—
3	1	$7.630337258 \times 10^{-3}$	$2.680231716 \times 10^{-2}$
3	2	$-4.779544711 \times 10^{-3}$	$-6.8263090 \times 10^{-4}$
3	3	$1.954532464 \times 10^{-4}$	$3.129206543 \times 10^{-4}$
4	0	0.1463823235	—
4	1	$-6.17186832 \times 10^{-3}$	$-2.571859603 \times 10^{-2}$
4	2	$6.155363522 \times 10^{-3}$	$7.868146794 \times 10^{-4}$
4	3	$-3.816451287 \times 10^{-4}$	$-6.1768351 \times 10^{-4}$
4	4	$1.808127835 \times 10^{-5}$	$2.432030673 \times 10^{-5}$

Table A3 Estimated normalized interior spherical harmonic coefficients with the 15×15 exterior gravity field as the source data (Sec. V.B)

Degree	Order	\bar{C}^i coefficients	\bar{S}^i coefficients
n	m	\bar{C}_{nm}^i	\bar{S}_{nm}^i
1	0	-0.4295276525	—
1	1	$8.133916332 \times 10^{-3}$	$2.304298826 \times 10^{-2}$
2	0	0.2823031966	—
2	1	$-8.517833720 \times 10^{-3}$	$-2.641976974 \times 10^{-2}$
2	2	$2.980730570 \times 10^{-3}$	$4.644044024 \times 10^{-4}$
3	0	-0.2001687525	—
3	1	$7.630316608 \times 10^{-3}$	$2.680233019 \times 10^{-2}$
3	2	$-4.779536997 \times 10^{-3}$	$-6.826332938 \times 10^{-4}$
3	3	$1.954535198 \times 10^{-4}$	$3.129178273 \times 10^{-4}$
4	0	0.146382383	—
4	1	$-6.171859018 \times 10^{-3}$	$-2.57186425 \times 10^{-2}$
4	2	$6.15536255 \times 10^{-3}$	$7.867954875 \times 10^{-4}$
4	3	$-3.816055679 \times 10^{-4}$	$-6.177141763 \times 10^{-4}$
4	4	$1.811164211 \times 10^{-5}$	$2.434616086 \times 10^{-5}$

$$\left(\frac{\partial}{\partial x} - i \frac{\partial}{\partial y}\right)^p f(z, r^2) = M^p f(z, r^2) = 2^p (x - iy)^p \frac{\partial^p f}{\partial (r^2)^p} = \tilde{g} \quad (\text{A30})$$

where the tilde denotes the complex conjugate. The power index of p appears due to the successive chain rule operations. For $m < q$, Eqs. (A28) and (A30) are used once the partial of the m th order is related to the zeroth order. Now, Eq. (A25) is substituted with $s = q - m$, $n' = n - m$, and $m' = 0$ to get

$$\begin{aligned} \left(\frac{\partial}{\partial x} + i \frac{\partial}{\partial y}\right)^s b_{n'm'}^i &= \left(\frac{\partial}{\partial x} + i \frac{\partial}{\partial y}\right)^{q-m} b_{n-m,0}^i \\ &= (-1)^{q-m} \left(\frac{1}{R^*}\right)^{q-m} b_{n-q,q-m}^i \end{aligned} \quad (\text{A31})$$

Thus, when $m < q$, the following expression is obtained by combining Eqs. (A28) and (A31):

$$\left(\frac{\partial}{\partial x} - i \frac{\partial}{\partial y}\right)^q b_{nm}^i = (-1)^{q-m} \frac{(n+m)!}{(n-m)!} \left(\frac{1}{R^*}\right)^q \tilde{b}_{n-q,q-m}^i \quad (\text{A32})$$

For Eq. (A26) to hold for any combination of m and q , Eq. (A26) is equated with Eq. (A32), with substitutions $n' = n + q$ and $m' = q - m$,

$$b_{n,-m}^i = (-1)^m \frac{(n-m)!}{(n+m)!} \tilde{b}_{n,m}^i \quad (\text{A33})$$

After rearranging Eqs. (A22) and (A23) to express the partial with respect to x and y , direct substitution yields the higher-order partials as

$$\begin{aligned} \frac{\partial^{\alpha+\beta+\gamma}}{\partial x^\alpha \partial y^\beta \partial z^\gamma} b_{nm}^i &= i^\beta \left(\frac{1}{R^*}\right)^{\alpha+\beta+\gamma} \sum_{j=0}^{\alpha+\beta} \frac{(-1)^{\alpha-j}}{2^{\alpha+\beta}} \\ &\times \frac{(n+m)!}{(n+m-\gamma-2j)!} L_{\alpha,\beta,j} b_{n-\alpha-\beta-\gamma,m+\alpha+\beta-2j}^i \end{aligned} \quad (\text{A34})$$

where $L_{\alpha,\beta,j}$ is defined by Cunningham [26] as

$$L_{\alpha,\beta,j} = \sum_{k=0}^j (-1)^k \binom{\alpha}{j-k} \binom{\beta}{k} \quad (\text{A35})$$

Equation (A34) is the final form of the partial of b_{nm}^i . Explicit expressions for the second-order partials are solved for the normalized interior gravity field and given in the next section.

D. Second-Order Partial of the Potential

The dynamics matrix as well as the partial derivatives of the acceleration with respect to the normalized interior spherical harmonic coefficients are presented in the next two sections. These parameters are required to compute the state transition matrix for OD purposes. Note that only five components are necessary to compute the second-order partial of the potential as the Laplace equation needs to be satisfied at all times.

$$\begin{aligned} \frac{\partial^2 U^i}{\partial x^2} &= \frac{1}{4} \frac{GM^*}{(R^*)^3} \left[\frac{\bar{C}_{nm}^i}{\bar{S}_{nm}^i} \right] \cdot \left[\sqrt{\frac{(2n+1)(n-m)!}{(2n-3)(n-m-4)!}} \tilde{b}_{n-2,m+2}^i \right. \\ &\quad - 2 \sqrt{\frac{(2n+1)(n+m)!}{(2n-3)(n+m-2)!} \frac{(n-m)!}{(n-m-2)!}} \tilde{b}_{n-2,m}^i \\ &\quad \left. + \sqrt{\frac{2(2n+1)(n+m)!}{(2-\delta_{2,m})(2n-3)(n+m-4)!}} \tilde{b}_{n-2,m-2}^i \right] \\ &\stackrel{m=1}{=} \frac{1}{4} \frac{GM^*}{(R^*)^3} \left[\frac{\bar{C}_{n,1}^i}{\bar{S}_{n,1}^i} \right] \cdot \left[\sqrt{\frac{(2n+1)(n-1)!}{(2n-3)(n-5)!}} \tilde{b}_{n-2,3}^i \right. \\ &\quad \left. - \sqrt{\frac{(2n+1)(n+1)!}{(2n-3)(n-3)!}} \left[3\Re\{\tilde{b}_{n-2,1}^i\} \right] \right. \\ &\quad \left. - \sqrt{\frac{(2n+1)(n+1)!}{(2n-3)(n-3)!}} \left[3\Im\{\tilde{b}_{n-2,1}^i\} \right] \right] \\ &\stackrel{m=0}{=} \frac{1}{2} \frac{GM^*}{(R^*)^3} \left[\frac{\bar{C}_{n,0}^i}{\bar{S}_{n,0}^i} \right] \cdot \left[\sqrt{\frac{1(2n+1)n!}{2(2n-3)(n-4)!}} \tilde{b}_{n-2,2}^i \right. \\ &\quad \left. - \frac{n!}{(n-2)!} \sqrt{\frac{(2n+1)}{(2n-3)}} \tilde{b}_{n-2,0}^i \right] \end{aligned} \quad (\text{A36})$$

$$\begin{aligned}
\frac{\partial^2 U^i}{\partial y \partial x} &\stackrel{m \geq 1}{=} \frac{1}{4} \frac{GM^*}{(R^*)^3} \left[\frac{-\tilde{S}_{nm}^i}{\tilde{C}_{nm}^i} \right] \cdot \left[\sqrt{\frac{(2n+1)(n-m)!}{(2n-3)(n-m-4)!}} \tilde{b}_{n-2,m+2}^i \right. \\
&\quad \left. - \sqrt{\frac{2}{(2-\delta_{2,m})}} \frac{(2n+1)(n+m)!}{(2n-3)(n+m-4)!} \tilde{b}_{n-2,m-2}^i \right] \\
&\stackrel{m=1}{=} \frac{1}{4} \frac{GM^*}{(R^*)^3} \left[\frac{-\tilde{S}_{n,1}^i}{\tilde{C}_{n,1}^i} \right] \cdot \left[\sqrt{\frac{(2n+1)(n-1)!}{(2n-3)(n-5)!}} \tilde{b}_{n-2,3}^i \right. \\
&\quad \left. + \sqrt{\frac{(2n+1)(n+1)!}{(2n-3)(n-3)!}} \left[\Re\{\tilde{b}_{n-2,1}^i\} \right] \right] \\
&\stackrel{m=0}{=} \frac{1}{2} \frac{GM^*}{(R^*)^3} \left[\frac{-\tilde{S}_{n,0}^i}{\tilde{C}_{n,0}^i} \right] \cdot \left[\sqrt{\frac{1}{2} \frac{(2n+1)n!}{(2n-3)(n-4)!}} \tilde{b}_{n-2,2}^i \right] \quad (A37)
\end{aligned}$$

$$\begin{aligned}
\frac{\partial^2 U^i}{\partial y^2} &\stackrel{m \geq 1}{=} -\frac{1}{4} \frac{GM^*}{(R^*)^3} \left[\frac{\tilde{C}_{nm}^i}{\tilde{S}_{nm}^i} \right] \cdot \left[\sqrt{\frac{(2n+1)(n-m)!}{(2n-3)(n-m-4)!}} \tilde{b}_{n-2,m+2}^i \right. \\
&\quad + 2 \sqrt{\frac{(2n+1)(n+m)!}{(2n-3)(n+m-2)!}} \frac{(n-m)!}{(n-m-2)!} \tilde{b}_{n-2,m}^i \\
&\quad \left. + \sqrt{\frac{2}{(2-\delta_{2,m})}} \frac{(2n+1)(n+m)!}{(2n-3)(n+m-4)!} \tilde{b}_{n-2,m-2}^i \right] \\
&\stackrel{m=1}{=} -\frac{1}{4} \frac{GM^*}{(R^*)^3} \left[\frac{\tilde{C}_{n,1}^i}{\tilde{S}_{n,1}^i} \right] \cdot \left[\sqrt{\frac{(2n+1)(n-1)!}{(2n-3)(n-5)!}} \tilde{b}_{n-2,3}^i \right. \\
&\quad \left. + \sqrt{\frac{(2n+1)(n+1)!}{(2n-3)(n-3)!}} \left[3\Im\{\tilde{b}_{n-2,1}^i\} \right] \right] \\
&\stackrel{m=0}{=} -\frac{1}{2} \frac{GM^*}{(R^*)^3} \left[\frac{\tilde{C}_{n,0}^i}{\tilde{S}_{n,0}^i} \right] \cdot \left[\sqrt{\frac{1}{2} \frac{(2n+1)n!}{(2n-3)(n-4)!}} \tilde{b}_{n-2,2}^i \right. \\
&\quad \left. + \frac{n!}{(n-2)!} \sqrt{\frac{(2n+1)}{(2n-3)}} \tilde{b}_{n-2,0}^i \right] \quad (A38)
\end{aligned}$$

$$\begin{aligned}
\frac{\partial^2 U^i}{\partial x \partial z} &\stackrel{m \geq 0}{=} \frac{1}{2} \frac{GM^*}{(R^*)^3} \left[\frac{\tilde{C}_{nm}^i}{\tilde{S}_{nm}^i} \right] \\
&\cdot \left[-\sqrt{\frac{(2n+1)(n-m)!}{(2n-3)(n-m-3)!}} (n+m) \tilde{b}_{n-2,m+1}^i \right. \\
&\quad \left. + \sqrt{\frac{2}{(2-\delta_{1,m})}} \frac{(2n+1)(n+m)!}{(2n-3)(n+m-3)!} \frac{(n-m)!}{(n-m-1)!} \tilde{b}_{n-2,m-1}^i \right] \\
&\stackrel{m=0}{=} \frac{GM^*}{(R^*)^3} \left[\frac{\tilde{C}_{n,0}^i}{\tilde{S}_{n,0}^i} \right] \cdot \left[-\sqrt{\frac{n(2n+1)n!}{2(2n-3)(n-3)!}} \tilde{b}_{n-2,1}^i \right] \quad (A39)
\end{aligned}$$

$$\begin{aligned}
\frac{\partial^2 U^i}{\partial y \partial z} &\stackrel{m \geq 0}{=} \frac{1}{2} \frac{GM^*}{(R^*)^3} \left[\frac{-\tilde{S}_{nm}^i}{\tilde{C}_{nm}^i} \right] \\
&\cdot \left[-\sqrt{\frac{(2n+1)(n-m)!}{(2n-3)(n-m-3)!}} (n+m) \tilde{b}_{n-2,m+1}^i \right. \\
&\quad \left. - \sqrt{\frac{2}{(2-\delta_{1,m})}} \frac{(2n+1)(n+m)!}{(2n-3)(n+m-3)!} \frac{(n-m)!}{(n-m-1)!} \tilde{b}_{n-2,m-1}^i \right] \\
&\stackrel{m=0}{=} \frac{GM^*}{(R^*)^3} \left[\frac{-\tilde{S}_{n,0}^i}{\tilde{C}_{n,0}^i} \right] \cdot \left[-\sqrt{\frac{n(2n+1)n!}{2(2n-3)(n-3)!}} \tilde{b}_{n-2,1}^i \right] \quad (A40)
\end{aligned}$$

$$\begin{aligned}
\frac{\partial^2 U^i}{\partial z^2} &= \frac{GM^*}{(R^*)^3} \left[\frac{\tilde{C}_{nm}^i}{\tilde{S}_{nm}^i} \right] \\
&\cdot \left[\sqrt{\frac{(2n+1)(n+m)!}{(2n-3)(n+m-2)!}} \frac{(n-m)!}{(n-m-2)!} \tilde{b}_{n-2,m}^i \right] \quad (A41)
\end{aligned}$$

E. Partial Derivative of Acceleration with Respect to \tilde{C}_{nm}^i and \tilde{S}_{nm}^i

$$\frac{\partial \ddot{x}}{\partial \tilde{C}_{nm}^i} = \frac{GM^*}{(R^*)^2} [-\bar{g}_1^i(n, m) \Re\{\tilde{b}_{n-1,m+1}^i\} + \bar{g}_2^i(n, m) \Re\{\tilde{b}_{n-1,m-1}^i\}] \quad (A42)$$

$$\frac{\partial \ddot{x}}{\partial \tilde{S}_{nm}^i} = \frac{GM^*}{(R^*)^2} [-\bar{g}_1^i(n, m) \Im\{\tilde{b}_{n-1,m+1}^i\} + \bar{g}_2^i(n, m) \Im\{\tilde{b}_{n-1,m-1}^i\}] \quad (A43)$$

$$\frac{\partial \ddot{y}}{\partial \tilde{C}_{nm}^i} = \frac{GM^*}{(R^*)^2} [-\bar{g}_1^i(n, m) \Im\{\tilde{b}_{n-1,m+1}^i\} - \bar{g}_2^i(n, m) \Im\{\tilde{b}_{n-1,m-1}^i\}] \quad (A44)$$

$$\frac{\partial \ddot{y}}{\partial \tilde{S}_{nm}^i} = \frac{GM^*}{(R^*)^2} [\bar{g}_1^i(n, m) \Re\{\tilde{b}_{n-1,m+1}^i\} + \bar{g}_2^i(n, m) \Re\{\tilde{b}_{n-1,m-1}^i\}] \quad (A45)$$

$$\frac{\partial \ddot{z}}{\partial \tilde{C}_{nm}^i} = \frac{GM^*}{(R^*)^2} [\bar{g}_3^i(n, m) \Re\{\tilde{b}_{n-1,m+1}^i\}] \quad (A46)$$

$$\frac{\partial \ddot{z}}{\partial \tilde{S}_{nm}^i} = \frac{GM^*}{(R^*)^2} [\bar{g}_3^i(n, m) \Im\{\tilde{b}_{n-1,m+1}^i\}] \quad (A47)$$

where

$$\begin{cases} \bar{g}_1^i(n, m) = \frac{1}{2} (1 + \delta_{0,m}) \sqrt{\frac{(2-\delta_{0,m})}{(2-\delta_{0,m+1})}} \frac{(2n+1)(n-m)!}{(2n-1)(n-m-2)!} \\ \bar{g}_2^i(n, m) = \frac{1}{2} \sqrt{\frac{(2-\delta_{0,m})}{(2-\delta_{1,m})}} \frac{(2n+1)(n+m)!}{(2n-1)(n+m-2)!} \\ \bar{g}_3^i(n, m) = \sqrt{\frac{(2n+1)}{(2n-1)}} (n+m)(n-m) \end{cases} \quad (A48)$$

F. List of Interior Spherical Harmonic Coefficients

The values of the interior spherical harmonic coefficients used to propagate the spacecraft dynamics in Sec. VI.B are listed. Many digits are retained to show the small discrepancies between the different methods. That is, not all of them are significant. For space purposes, only the lower-degree terms (up to degree and order four) are provided. Higher-degree and higher-order terms can be provided on request.

Acknowledgments

Y. Takahashi and D. J. Scheeres acknowledge funding from the OSIRIS-REx mission through a grant from the University of Arizona. The authors would like to acknowledge funding from the Jet Propulsion Laboratory and thank Theodore Sweetser for his support of this research.

References

- [1] Miller, J. K., Konopliv, A. S., Antreasian, P. G., Bordi, J. J., Chesley, S., Helfrich, C. E., Owen, W. M., Wang, T. C., Williams, B. G., Yeomans, D. K., and Scheeres, D. J., "Determination of Shape, Gravity, and Rotational State of Asteroid 433 Eros," *Icarus*, Vol. 155, No. 1, 2002,

- pp. 3–17.
doi:10.1006/icar.2001.6753
- [2] Takahashi, Y., and Scheeres, D. J., “Small Body Surface Gravity Field Estimation from Orbit Determination,” *34th Annual AAS Guidance and Control Conference*, American Astronautical Society Paper 11-053, Springfield, VA, 2011.
 - [3] Takahashi, Y., and Scheeres, D. J., “Rapid Characterization of a Small Body via Slow Flybys,” *20th AAS/AIAA Space Flight Mechanics Meeting*, AAS Paper 10-244, 2010.
 - [4] Takahashi, Y., and Scheeres, D. J., “Analytical Estimates of Gravity Field via Flybys,” *AAS/AIAA Space Flight Mechanics Meeting*, Toronto, AIAA Paper 2010-8372, 2010.
 - [5] Scheeres, D. J., Gaskell, R., Abe, S., Barnouin-Jha, O., Hashimoto, T., Kawaguchi, J., Kubota, T., Saito, J., Yoshikawa, M., Hirata, N., Mukai, T., Ishiguro, M., Kominato, T., Shirakawa, K., and Uo, M., “The Actual Dynamical Environment About Itokawa,” *AIAA/AAS Astrodynamics Specialist Meeting*, AIAA Paper 2006-6661, Aug. 2006.
 - [6] Konopliv, A. S., Miller, J. K., Owen, W. M., Yeomans, D. K., Giorgini, J. D., Garmier, R., and Barriot, J.-P., “A Global Solution for the Gravity Field, Rotation, Landmarks, and Ephemeris of Eros,” *Icarus*, Vol. 160, No. 2, 2002, pp. 289–299.
doi:10.1006/icar.2002.6975
 - [7] Garmier, R., Barriot, J.-P., Konopliv, A. S., and Yeomans, D. K., “Modeling of the Eros Gravity Field as an Ellipsoidal Harmonic Expansion from the NEAR Doppler Tracking Data,” *Geophysical Research Letters*, Vol. 29, No. 8, 2002, p. 1231.
doi:10.1029/2001GL013768
 - [8] Zuber, M. T., Smith, D. E., Cheng, A. F., Garvin, J. B., Aharonson, O., Cole, T. D., Dunn, P. J., Guo, Y., Lemoine, G. G., Neumann, G. A., Rowlands, D., and Torrence, M. H., “The Shape of 433 Eros from the NEAR-Shoemaker Laser Rangefinder,” *Science*, Vol. 289, Sept. 2000, pp. 2097–2101.
doi:10.1126/science.289.5487.2097
 - [9] Werner, R. A., and Scheeres, D. J., “Exterior Gravitation of a Polyhedron Derived and Compared with Harmonic and Mascon Gravitation Representations of Asteroid 4769 Castalia,” *Celestial Mechanics and Dynamical Astronomy*, Vol. 65, Aug. 1997, pp. 314–344.
doi:10.1007/BF00053511
 - [10] Romain, G., and Jean-Pierre, B., “Ellipsoidal Harmonic Expansions of the Gravitational Potential: Theory and Application,” *Celestial Mechanics and Dynamical Astronomy*, Vol. 79, Nov. 2001, pp. 235–275.
doi:10.1023/A:1017555515763
 - [11] Gottlieb, P., “Estimation of Local Lunar Gravity Features,” *Radio Science*, Vol. 5, No. 2, 1970, pp. 301–312.
doi:10.1029/RS005i002p00301
 - [12] Beylkin, G., and Cramer, R., “Toward Multiresolution Estimation and Efficient Representation of Gravitational Fields,” *Celestial Mechanics and Dynamical Astronomy*, Vol. 84, 2002, pp. 87–104.
doi:10.1023/A:1019941111529
 - [13] Jones, B. A., “Efficient Models for the Evaluation and Estimation of the Gravity Field,” Ph.D. Dissertation, Aerospace Engineering Sciences, Univ. of Colorado at Boulder, Boulder, CO, 2010.
 - [14] Cangahuala, L. A., “Augmentations to the Polyhedral Gravity Model to Facilitate Small Body Navigation,” *15th AAS/AIAA Spaceflight Mechanics Meeting*, Copper Mountain, Colorado, American Astronomical Society Paper 05-4185, 2005.
 - [15] Broschart, S. B., “Close Proximity Spacecraft Maneuvers near Irregularly Shaped Small-Bodies: Hovering, Translation, and Descent,” Ph.D. Dissertation, Aerospace Engineering, Univ. of Michigan, Ann Arbor, Michigan, 2006.
 - [16] Cangahuala, L. A., Broschart, S. B., Acikmese, B., Mandic, M., Blackmore, L., Riedel, E., Bayard, D., and Wallace, M., “GNC Trades for Touch-and-Go Sampling at Small Bodies,” *34th Annual AAS Guidance and Control Conference*, American Astronautical Society Paper 11-057, Springfield, VA, 2011.
 - [17] Kaula, W. M., *Theory of Satellite Geodesy*, Blaisdell, Waltham, MA, 1966, pp. 1–11, Chap. 1.
 - [18] Lundberg, J. B., and Schutz, B. E., “Recursion Formulas of Legendre Functions for use with Nonsingular Geopotential Models,” *Journal of Guidance, Control, and Dynamics*, Vol. 11, 1988, pp. 31–38.
doi:10.2514/3.20266
 - [19] Brillouin, M., “Equations aux Dérivées Partielles du 2e Ordre. Domaines à Connexion Multiple. Fonctions Sphériques non Antipodes,” *Annales de l'Institut Henri Poincaré*, Vol. 4, No. 2, 1933, pp. 173–206.
 - [20] Park, R. S., Werner, R. A., and Bhaskaran, S., “Estimating Small-Body Gravity Field from Shape Model and Navigation Data,” *Journal of Guidance, Control, and Dynamics*, Vol. 33, Jan.–Feb. 2010, pp. 212–221.
doi:10.2514/1.41585
 - [21] Werner, R. A., “Evaluating Descent and Ascent Trajectories near Non-Spherical Bodies,” Jet Propulsion Lab., California Inst. of Technology TR, Pasadena, CA, 2010.
 - [22] Takahashi, Y., and Scheeres, D., “Surface Gravity Fields for Asteroids and Comets,” *22nd AAS/AIAA Space Flight Mechanics Meeting*, AAS Paper 12-224, 2012.
 - [23] MacRobert, T. M., *Spherical Harmonics: An Elementary Treatise on Harmonic Functions with Applications*, 2nd ed., Dover, New York, 1948, pp. 72–84, Chap. 4.
 - [24] Werner, R. A., “Spherical Harmonic Coefficients for the Potential of a Constant-Density Polyhedron,” *Computers and Geosciences*, Vol. 23, No. 10, 1997, pp. 1071–1077.
doi:10.1016/S0098-3004(97)00110-6
 - [25] Hotine, M., *Mathematical Geodesy, ESSA Monograph 2*, Environmental Science Services Administration, U.S. Department of Commerce, 1969, Chap. 21.
 - [26] Cunningham, L. E., “On the Computation of the Spherical Harmonic Terms Needed During the Numerical Integration of the Orbital Motion of an Artificial Satellite,” *Celestial Mechanics*, Vol. 2, Aug. 1970, pp. 207–216.
doi:10.1007/BF01229495